

Simulation of laser cooling by the bichromatic force

Xiang Hua, Christopher Corder, and Harold Metcalf

Physics and Astronomy, Stony Brook University, Stony Brook, New York 11794-3800, USA

(Received 22 March 2016; published 10 June 2016)

The bichromatic force allows laser cooling using stimulated processes only. We provide details of our simulations of the bichromatic force when the effects of spontaneous emission are suppressed by restricting the atom-light interaction time to be short enough that there cannot be a significant number of spontaneous emission events. This short interaction time requires that the simulation include dynamics of the atomic motion through the light field that is coupled to the internal state dynamics that determine the force on the atom. The simulation is first tested with several standard optical field configurations to confirm its accuracy. Then the results, using conditions that match our experiment, are presented and compared with our measurements. The simulation shows that the resolution of the experiment greatly obscures the degree of cooling. Our simulation predicts an observed velocity distribution reduced by up to a factor of 4 in width over a time comparable to the excited state lifetime. This technique can allow the direct laser cooling of atoms and molecules without closed cycling transitions.

DOI: [10.1103/PhysRevA.93.063410](https://doi.org/10.1103/PhysRevA.93.063410)

I. INTRODUCTION AND BACKGROUND

This paper describes a numerical simulation of the optical forces that can produce laser cooling using the bichromatic force (BF) [1–3]. Its primary purpose is to provide support for the simulation assertions in Ref. [4]. Our interest comes from the fact that the BF derives from purely stimulated processes, and cooling without spontaneous emission has been a topic of interest for us for several years [4–6]. It turns out that spontaneous emission serves only to help define a direction for the BF over long interaction times [7,8]. The entire simulation is for a two-level atom with excited state lifetime $\tau \equiv 1/\gamma$ and transition wavelength $\lambda \equiv 2\pi/k$. For our $2^3S_1 \leftrightarrow 3^3P_2$ transition in He, $\lambda = 389$ nm and $\tau = 106$ ns.

The calculation begins by establishing the light field. This requires both the atomic position $z(t)$ in the bichromatic plane standing waves with $\vec{k} = k_z$ to determine the relative optical phase, and the atomic velocities $v_z(t)$ to determine the Doppler shifts and hence the detuning for the Hamiltonian \mathcal{H} . The strength of the atom-light interaction is defined by the Rabi frequency Ω for each of the four traveling-wave beams needed to produce the BF.

Knowledge of the light field seen by the atoms enables the solution of the optical Bloch equations (OBEs), with damping, to determine the atomic internal state in the form of the density matrix $\rho(t)$ [9]. Then the force is found from $\text{tr}[\rho(t)\nabla\mathcal{H}]$, the atomic velocity $v_z(t)$ and position $z(t)$ are updated classically with the resulting velocity and path changes in a short time interval (typically ps), and the calculation is iterated on the ps time scale.

Simulating an experiment requires calculation of the atomic trajectories since these determine the outcome of the measurements. Thus we calculate atomic trajectories $[z(t), v_z(t)]$ over a fixed time span of the evolution of $\rho(t)$. Note that this differs from the more commonly used “dragged atom” approach ($v_z = \text{constant}$) that produced force vs velocity curves [1,3]. Instead, we update $v_z(t)$, $z(t)$, and the field, after each time interval.

The code is fundamentally different from earlier versions of similar calculations (see Fig. 4.3 of Ref. [10] and Refs. [1–3,11–13]) because it takes into account the initial

conditions. In those previous calculations, the OBE’s were allowed to iterate for a long enough time for $\rho(t)$ to reach a steady state in the light field at a fixed velocity, and then the force was calculated from the result. Here we specify the initial values of z , v_z , starting time t_0 , and optical phase, and then solve for the time-dependent force using $\text{tr}[\rho(t)\nabla\mathcal{H}]$. An ensemble of atoms with different initial conditions is treated, and the temporal evolution is calculated for relatively short interaction times. We do this because we want to simulate the absence of spontaneous emission since both the calculation and the experiment run for times comparable to or less than 2τ [4,6].

For most of the calculational results presented here, a set of initial parameters is chosen and the trajectories are calculated for an ensemble of atoms characterized by a pre-selected range of one of the initial parameters. The resulting set of trajectories is grouped and arranged to show the effects of the BF on the velocity distribution of the ensemble. Their spatial paths have also been calculated for detailed comparison with our measurements.

II. TESTING THE CODE

The first of several tests of the code used a traveling wave of a single frequency ω_ℓ detuned from the atomic frequency ω_a by $\delta \equiv \omega_\ell - \omega_a \approx 15\gamma \approx +2\pi \times 22.5$ MHz. In a traveling wave, the position of the atoms has no bearing on the results so the calculation uses an ensemble of equally spaced starting velocities. Figure 1 shows that atoms having initial velocity $+15\gamma/k$ experience the largest force at the start of the evolution because their Doppler shifts just compensate the blue detuning. Those with smaller velocities are accelerated into resonance where they experience a large force at later times (steepest slopes in Fig. 1 at $v = +15\gamma/k$), and those with higher velocities experience less acceleration. Changing the sign of the detuning or the direction of propagation of the light simply translated these curves vertically or reflected them about the horizontal.

For the second set of tests we examined the velocity trajectories in a single-frequency standing wave. Figure 2

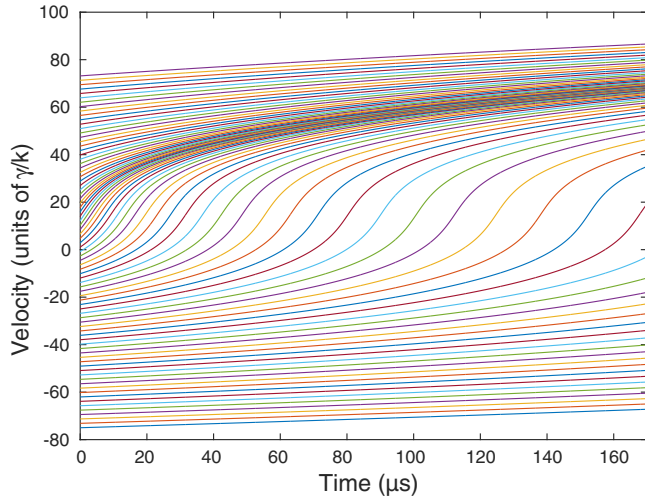


FIG. 1. Atomic motion in a traveling wave. These curves show the velocity vs time for atoms with different starting velocities in a single traveling wave detuned by $\delta \approx +2\pi \times 22.5$ MHz (blue) and $\Omega = \sqrt{3/2}\delta$. For atoms with $v = 15\gamma/k$ whose Doppler shifts cancel δ , most of the velocity change occurs in $\sim 10\mu s$ whereas the time runs for $160\mu s$, much longer than the actual experiment.

shows plots of atomic velocities vs time in single standing waves with $\delta \approx \pm 15\gamma \approx \pm 2\pi \times 22.5$ MHz for a range of initial velocities, and $\Omega = \sqrt{3/2}|\delta|$ [see below and Eq. (2) for discussion of this choice of Ω]. A starting position is well defined in a standing wave, but the plots for a range of starting positions all show similar properties.

As expected, atoms with kinetic energies below the magnitude of the light shifts were confined to the channels between the standing wave nodes or antinodes, depending on detuning [14]. For atomic velocity $\tilde{v} \equiv v/(\gamma/k)$ the kinetic energy is

$$E_K = \frac{Mv^2}{2} = \frac{M}{2} \left(\frac{\tilde{v}\gamma}{k} \right)^2 = \hbar\gamma \frac{\tilde{v}^2}{4} \frac{\gamma}{\omega_r}, \quad (1)$$

where $\omega_r \equiv \hbar k^2/2M \approx 2\pi \times 329$ kHz is the recoil frequency of the $2^3S_1 \leftrightarrow 3^3P_2$ transition of interest here.

Thus confinement requires $\tilde{v} < \alpha\sqrt{\omega_r\delta/\gamma^2}$ where the numerical factor $\alpha \approx 1.8$ can be found by setting this $E_K \leq \hbar\omega_{LS}$ [see Eq. (2)], using the full Ω without the $\sqrt{2}$. This condition

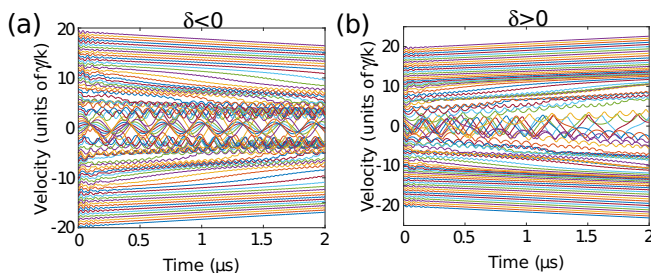


FIG. 2. The evolution of atomic velocities in a single frequency standing wave detuned by $\delta \approx \pm 2\pi \times 22.5$ MHz. The central regions show that atoms with starting velocities between $\tilde{v} = \pm 3.3$ are confined and exhibit oscillatory velocities.

is $\tilde{v} < 3.3$, and indeed atoms with starting velocities between $\tilde{v} = \pm 3.3$ are shown in Fig. 2 to be confined, and exhibit oscillatory velocities and positions. Only those paths that cross $v_z = 0$ represent confined atoms.

For velocities outside this range, the unconfined atoms are traveling in an optical molasses. The difference between Figs. 2(a) and 2(b) is the sign of δ . For red (blue) detuning, the resulting optical molasses cools (heats) the atoms so that their velocities decrease (increase) as shown, both above and below the middle of the plots where $|\tilde{v}| > 3.3$. The molasses cooling time at $\delta \approx -15\gamma$ and $\Omega = \sqrt{3/2}|\delta| \approx 18\gamma$ is $\sim 10\mu s$, and therefore cooling (heating) is noticeable but not significant on this $2\text{-}\mu s$ time scale. Their slight wobble arises from their motion over the potential hills and valleys (more rapid oscillations at higher speeds).

With these two quite successful tests of the code, we are confident in extending it to the case of simultaneous red- and blue-detuned standing waves (four beams) that are used to implement the BF.

III. THE BICHROMATIC FORCE

A good introduction to the BF is found in Ref. [6], but a short review is given here. It is implemented with standing waves of two different frequencies, usually symmetrically detuned from the atomic resonance frequency ω_a by $\pm\delta$, and typically $|\delta| \gg \gamma$ [1]. The standing waves are spatially offset by $\lambda/8$, corresponding to a spatial phase offset of $\pi/4$ of the intensity distribution whose spatial period is $\lambda/2$ [1]. Here the required, exact, dressed state crossings [3] occur because one of the standing waves has a node and the Rabi frequency of the other one is not at its maximum; instead it is $\Omega/\sqrt{2}$. For the two-level atom of our model, the light shift is thus

$$\hbar\omega_{LS} = \frac{\hbar}{2} \left(\sqrt{\left(2 \times \frac{\Omega}{\sqrt{2}} \right)^2 + \delta^2} - \delta \right), \quad (2)$$

where the factor 2 multiplying $\Omega/\sqrt{2}$ arises because there are two beams making up the standing wave and Ω is the value for each of these beams [9,15]. The light shift $\hbar\omega_{LS}$ then causes the exact crossing when it is half the splitting between adjacent dressed states, namely $\omega_{LS} = |\delta|/2$, and this occurs at $\Omega = \sqrt{3/2}|\delta|$.

Our simulation of the BF is based on the calculations described above, in the presence of the four laser beams needed to make the two standing waves. It is important to re-emphasize that the details of the trajectories differ significantly with changes of the initial starting values of the atomic parameters, but in all cases converge to the results predicted by the usual models of the BF. Some of the ideas of this simulation are introduced in Ref. [6].

As a first example of the simulation, we calculate the velocity trajectories that result from all four beams under conditions that optimize the BF for $\delta = \pm 15\gamma$, namely, spatial phase offset of the standing waves $= \lambda/8$, and $\Omega = \sqrt{3/2}|\delta|$. We run this for $3\mu s \approx 28\tau$ so that the full effects of spontaneous emission come into play. Figure 3(a) shows that these trajectories bunch tightly in velocity space at a bit below $v = -7.5\gamma/k$ because the force profile has some graded decline near its range limit of $\pm\delta/2k$ [1,3].

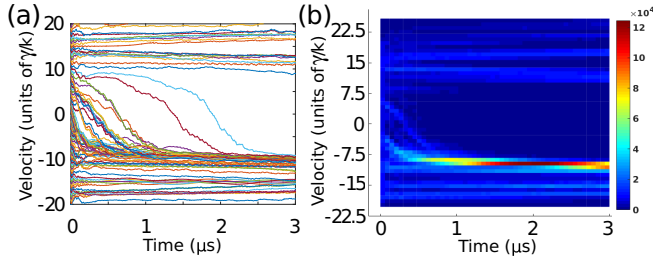


FIG. 3. (a) Plot of velocity trajectories and (b) trajectory densities for the BF. The time span is 3 μs , the detunings are $\delta = \pm 15\gamma$, and $\Omega = \sqrt{3/2}|\delta|$. Over such a long time, $\sim 28\tau$, there can be many spontaneous emissions and the plots show substantial velocity space compression just below $v = -7.5\gamma/k$.

To ease interpretation of such plots we have also plotted the trajectory density. This involves running the calculation for a much larger number of equally spaced, initial velocity values and binning them in velocity and time. This is shown in Fig. 3(b) for 3240 initial velocity values so each bin starts with 65 trajectories. The bin width is 60 ns to make the grid “square” on this scale, and the number of trajectories in each bin is counted and plotted as the third dimension (here indicated by color). Both of these plots display strong cooling to just below $v = -|\delta|/2k$ as expected. For a spatial offset of the standing waves of $3\lambda/8$, the force would be reversed and the cooling would be toward $v = +|\delta|/2k$. For these conditions, all starting positions lead to nearly the same final velocity distribution.

A. Velocity space trajectories

We can now examine the short-time dependence (comparable to τ) of interest to our experiment more carefully. Spontaneous emission cannot be prevented, but in our experiment its effect is minimized by using a very short interaction time. For the BF, the characteristic cooling time is $\pi/4\omega_r \approx 380$ ns [4]. In the experiment, the laser beams are carefully controlled so that the average interaction time can be just a few τ , corresponding to ≈ 1.5 spontaneous emission cycle times [4].

Our simulation results for velocity trajectories in a bichromatic field during a 300-ns time interval are shown in Fig. 4. The trajectories clearly show a strong coalescence near $v = -|\delta|/2k \approx -7.5\gamma/k$ as expected for the BF [4,6]. All previous steady-state force calculations and simulations show that the BF essentially vanishes at $v = \pm\delta/2k$ so that atoms accumulate near this value. Even in the short time of this calculation, they are collected from a wide region of velocity space spanning $v = \pm\delta/2k$ and are compressed into a narrow region near the velocity limit.

Each plot in Fig. 4 has 81 equally spaced starting velocities, again using standing waves of spatial phase offset equal $\lambda/8$, $\delta = \pm 15\gamma$ and $\Omega = \sqrt{3/2}|\delta|$. They have different starting parameters indicated by $[z_0, t_0]$, where the potential minimum for the blue (red) standing wave is at $z_0 = 7\lambda/16$ ($z_0 = 5\lambda/16$). For Fig. 4(a) these starting points are $[0, 0]$, for Fig. 4(b) they are $[\lambda/8, 0]$, for Fig. 4(c) they are $[0, \pi/(4|\delta|)]$, and for Fig. 4(d) they are $[\lambda/8, \pi/(4|\delta|)]$. (Note that the starting position is not to be confused with the standing wave spatial

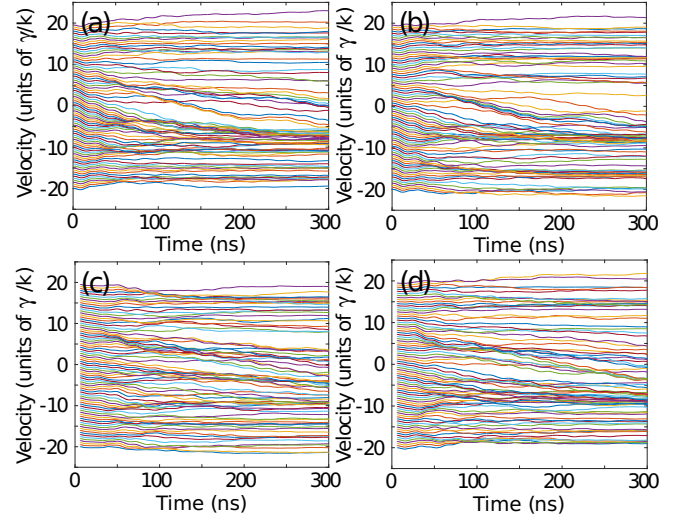


FIG. 4. Trajectories on the 300-ns time scale for the BF. These plots span only 300 ns, unlike the much longer times of Figs. 1–3, but are closer to the experimental interaction time. Each plot shows 81 velocity trajectories from the same bichromatic field (spatial phase offset of the standing waves = $\lambda/8$, $\delta = \pm 15\gamma$ and $\Omega = \sqrt{3/2}|\delta|$) but having different starting parameters. For initial conditions of the $[z_0, t_0]$, plot (a) is $[0, 0]$, (b) is $[\lambda/8, 0]$, (c) is $[0, \pi/(4|\delta|)]$, and (d) is $[\lambda/8, \pi/(4|\delta|)]$.

phase offset.) Quite comparable velocity space compression occurs even though the individual paths differ.

Figure 5(a) shows the trajectory density with the same laser parameters as Fig. 4 with the same 3240 equally spaced initial velocities but with six starting positions summed. The trajectories vary noticeably, but not drastically, with starting position, and this plot is a sum of six plots with $z_0 = \lambda/12, \lambda/6, \lambda/4 \dots$ in steps of $\lambda/12$, but all with starting $t_0 = 0$. Varying t_0 results in different trajectories but the final distributions are very similar. In some cases these plots are easier to see in three dimensions and from a different perspective, as shown in Fig. 5(b). Note the very strong cooled-atom peak $5\gamma/k$ wide and just over 1200 points high centered at $v = -|\delta|/2k \approx -7.5\gamma/k$. It comes from atoms collected over a velocity range of $\pm\delta/2k$ as before, and represents a velocity change of up to $\approx 35v_r$, where $v_r \equiv \hbar k/M$ is the recoil velocity.

In addition to the very strong cooled-atom peak, there are small but distinct, narrow features near $v = \pm\delta/k = \pm 15\gamma/k$. At these velocities, two traveling waves from opposite directions and opposite detunings are Doppler shifted into atomic resonance. Depending on binning, these features often appear to be doublets corresponding to peaks slightly detuned from exact Doppler-shifted resonance. Since the light intensity is high, we attribute these features to the Doppler resonances described in Refs. [9,16,17], especially since they vanish at lower intensities.

B. Experimental considerations

The magnetic substructure of the two states connected by the laser light needs to be carefully considered [4]. The 2^3S_1 ground state has three sublevels, and the 3^3P_2 excited state has

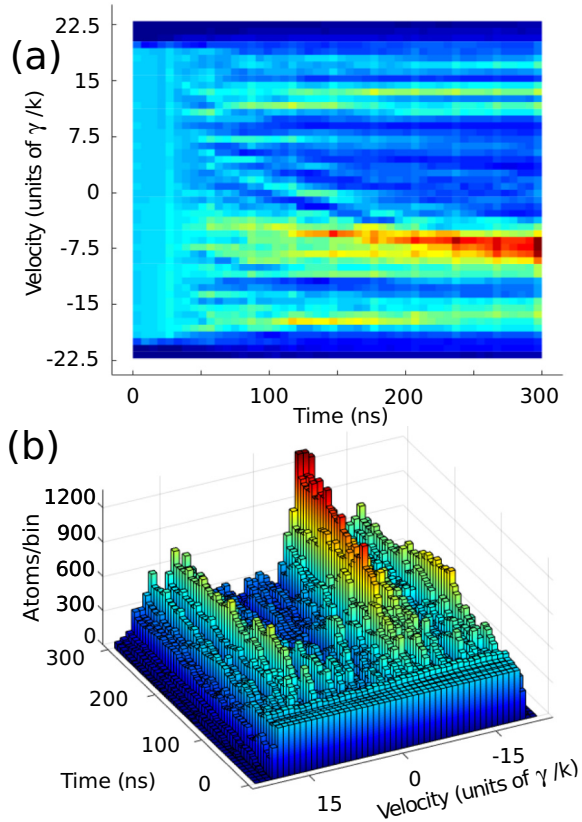


FIG. 5. (a) The atomic trajectory density in velocity space calculated with the four traveling waves used to produce the BF. The laser parameters are the same as Fig. 4, and the bins have summed trajectories with starting positions from $z_0 = \lambda/12$ to $z_0 = \lambda/2$ in steps of $\lambda/12$ (starting times all zero). (b) The 3D atomic trajectory density for the same calculation as (a). Note that the effective cooling time is approximately a few hundred ns as estimated below. Also, there is little change in the earliest times, but there are noticeable changes by 30 ns, corresponding to a few full cycles for the Rabi frequency of $\approx 2\pi \times 27$ MHz.

five sublevels. (Choosing an excited 3P state with $J = 1$ or $J = 0$ would result in fewer atoms interacting with the light because of the selection rules, since we assume that all three magnetic sublevels of the ground state are equally populated by the He source.) Therefore a given light intensity driving the $2^3S_1 \leftrightarrow 3^3P_2$ transition results in different Rabi frequencies because of the different Clebsch-Gordan coefficients for the different connected sublevel pairs. Linearly polarized light driving $\Delta M_J = 0$ transitions produces less variation than other choices, so that is used. The ratio of the Rabi frequencies is then $\sqrt{3} : 2 : \sqrt{3}$. Since there is no way for us to select a single transition experimentally, we need to compromise on choosing the experimental laser intensity.

To simulate the effect of the multiple sublevels on the velocity distribution, we combine the simulation results for two values of Ω . In Fig. 6 we plot calculated results similar to those of Fig. 5. Figure 6(a) is for $\Omega = 1.17 |\delta|$ and Fig. 6(b) is for $\Omega = 1.35 |\delta|$. Figures 6(c) and 6(d) are the 2:1 weighted sum of (a) and (b), plotted similarly to Fig. 5. The ratio of the Rabi frequencies is $1.154 \approx 2/\sqrt{3}$ and the weight of Fig. 6(a) is

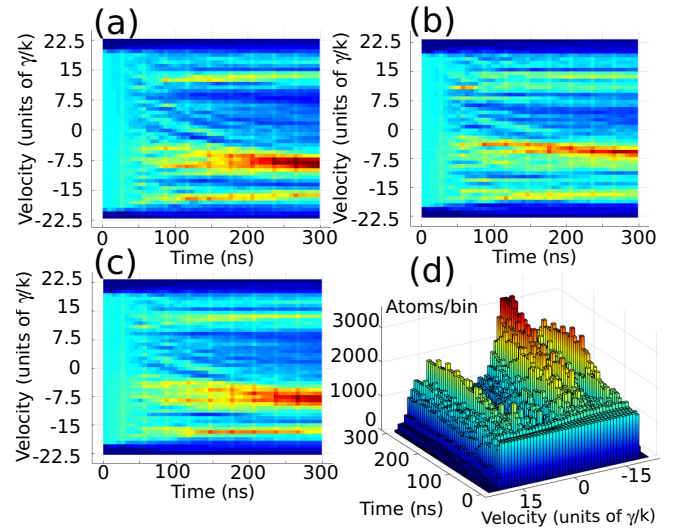


FIG. 6. Trajectory density plots with the same laser parameters and starting position averages as in Fig. 5. Panel (a) has $\Omega = 1.17 |\delta|$ and (b) has $\Omega = 1.35 |\delta|$. Neither is optimum but their ratio is $\approx 2/\sqrt{3}$ corresponding to the actual Clebsch-Gordan coefficients. Panel (c) is a 2:1 weighted sum of (a) and (b) corresponding to the sublevel multiplicity, and panel (d) is a 3D view of panel (c).

twice that of Fig. 6(b) in the sums shown in Figs. 6(c) and 6(d) to simulate the actual atomic structure. All four parts of Fig. 6 have a sum over the same set of starting positions z_0 , and have starting times $t_0 = 0$. The result is that Figs. 6(c) and 6(d) are very similar to Fig. 5, but slightly smeared.

Our experimental choice is to vary the light intensity over a wide range that includes the optimum Ω for each transition [4]. Thus our measurements are shown as a plot of the final atomic spatial distribution at the detector vs Rabi frequency [4,6].

C. Comparison with experiment

To compare our simulation results with these measurements, we need to calculate the atomic spatial distribution at the detector. In our experiment, atoms in a beam of metastable He (2^3S_1) cross the laser beams, carefully imaged to an (adjustable) sub-mm size, at 90° , and then fly freely for 63 cm to an imaging detector (see Ref. [6]). We measure cooling by the BF in the direction transverse to the atomic beam by measuring changes of the atomic spatial distribution at the detector (initially uniform). Since the laser and atomic beams cross very close to the $500 \mu\text{m}$ source aperture, and the atoms spread very little in the few hundred μm interaction region, we approximate the source as a point. Then the calculated transverse velocity distribution at the exit of the light field as shown in Fig. 6(c) or 6(d) is readily transformed to the spatial distribution at the detector.

However, in calculating (or measuring) the atomic velocity distribution at the detector there is a further complication [4,6]. The longitudinal velocity distribution of the atomic beam is centered at ≈ 1000 m/s but has a full width at half maximum (FWHM) of ≈ 400 m/s. Thus the 1000-m/s atoms with a final transverse velocity of $+|\delta|/2k \sim 4.3$ m/s are displaced by 2.7 mm at the detector. But the 400-m/s range of longitudinal velocities causes those atoms with a given

transverse velocity to be spread over more than 1 mm FWHM at the detector. Moreover, atoms with different longitudinal velocities have different interaction times in the laser beams. The consequences of this spreading is one of the primary experimental complications that our simulation is challenged to resolve.

Velocity distributions such as those in Fig. 6(c) or 6(c) with two Rabi frequencies having the same 2:1 weight (see Sec. III B), but also weighted by the measured longitudinal velocity distribution, are used to calculate the spatial distribution of atoms for comparison with the measurements. The measurements shown in Fig. 7(a) can be compared with the result of such a calculation as shown in Fig. 7(b). Note that the effect of the longitudinal velocity distribution is to smear the spatial distribution considerably and thereby reduce our resolution. Deconvolution doesn't help much because of the large size of the smearing compared with the features of interest—the FWHM of the large feature near 5 mm is ≈ 2 mm, corresponding to $>5\gamma/k \approx 3$ m/s.

Nevertheless, at this point we can compare the simulation results with the measurements. In Figs. 7(a) and 7(b) we see clear qualitative and some quantitative agreement in the region where the Rabi frequencies Ω are comparable. To do this, first note that the measured Ω of Fig. 7(a) depends on the accuracy of the power meter and on the geometrical corrections arising from the beam shape and intensity profile. Clearly the two plots would look much more alike if the vertical axis of Fig. 7(a) were scaled down by $\approx 12\%$, and this is not unreasonable considering the experimental uncertainties. Then the upper region of Fig. 7(a) is considered to have $\Omega \approx 21\gamma$ and is to be compared with the region near $\Omega \approx 21\gamma$ in Fig. 7(b).

The dominant features of Figs. 7(a) and 7(b) are the strong depletions of atoms near $v = -5$ to $+3$ m/s and the large accumulation near $v = +4$ to $+10$ m/s, each of which spreads over a $>30\%$ range of Ω 's. This is the region where the BF is strong for the transitions between the two pairs of magnetic

sublevels whose Ω 's differ by $>15\%$. For $\delta = \pm 16.7\gamma$ where the experiments were done, this corresponds well with $\Omega = \sqrt{3/2} |\delta| \approx 20.5\gamma$. These features occur without loss of atoms in the target region of $v = +4$ to $+10$ m/s suggesting that there is no force at these velocities $> \pm \delta/2k$, as predicted in Ref. [3].

For a more careful comparison of the simulation results with the measurements, we have taken line profiles from the $\Omega \approx 24\gamma$ region of Fig. 7(a) and $\approx 21\gamma$ of Fig. 7(b) [near the top of (a) and at 20γ of (b)]. These are plotted in Fig. 7(c), with background subtracted for the upper one (measurements). To begin, the dressed atom model of the BF predicts that about 1/4 of the atoms will be pushed in a direction opposite to the other 3/4, and that shows clearly in the two peaks of both parts of Fig. 7(c) [3,6]. The wide valley between these peaks spanning $v = -5$ to $+3$ m/s corresponds to $\approx \pm \delta/2k = 9.7$ m/s as expected from the velocity range of the BF [3,6].

In our experiment [Fig. 7(a)] the atoms with initial velocities in the wide range from $v = -5$ to $v = +10$ m/s have been cooled into the narrower range from $v = +4$ to $+10$ m/s. However, comparison of Fig. 7(b) with Figs. 6(c) and 6(d) strongly supports our claim that the measured width of the final spatial distribution is enlarged considerably by the effects of the longitudinal velocity spread, and that measuring the transverse velocity distribution directly would produce a much smaller width.

Thus the velocity space compression, and hence the cooling, is stronger than suggested by Fig. 7(a). By contrast, the wide valley in the region $v = -5$ to $+3$ m/s is NOT broadened by the effects of the longitudinal velocity distribution because the atoms are simply not there. Thus we feel that the simulation results in Figs. 6(c) and 6(d) more accurately represent the final velocity distribution achieved in the experiment and demonstrate compression by a factor of 3.

The compromise of the choice of Rabi frequencies resulting from the multiple transition strengths also has the effect of reducing the effectiveness of cooling, as seen by comparing

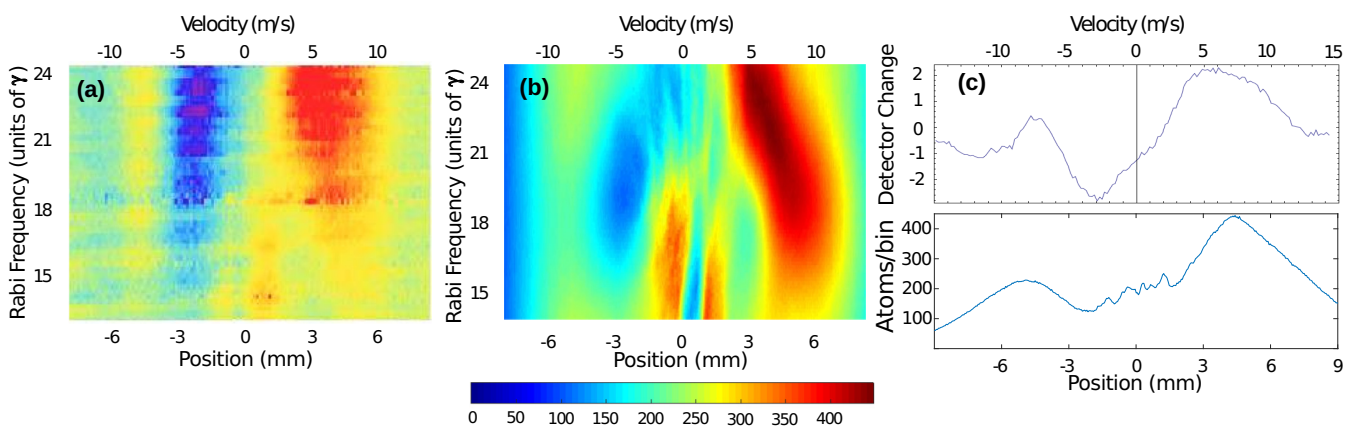


FIG. 7. Comparison of measurements and simulation. The horizontal axes are the positions on the detector corresponding to transverse atomic velocities, the vertical axes are the Rabi frequencies in units of γ , and the atomic density at the detector is indicated by the colors. (The transverse velocity values above each plot are for the case of longitudinal velocity of 1000 m/s.) (a) Shows the measured results after ≈ 220 ns and its vertical axis corresponds to the transition between $M_J = \pm 1$ sublevels. (b) Shows the output of the simulation, including the effects of the two different Rabi frequencies for the same light field. The qualitative agreement is quite good and there is significant quantitative agreement as well. The detuning for both parts is $\delta = \pm 2\pi \times 25$ MHz $\approx \pm 16.7\gamma$. (c) Shows the atomic distribution profile from particular sections of (a) and (b) (upper and lower curves, respectively). The background is subtracted for the upper (experimental) curve of (c). See text for details.

Fig. 6 with Fig. 5. For a single transition at the optimum Rabi frequency, Fig. 5 shows a fourfold velocity space compression whereas the compression of Fig. 6 is only threefold. This difference corresponds to a factor of 16 vs 9 in temperature.

We can contrast the result of BF cooling with what is possible from a Doppler molasses on the same transition. The Doppler cooling limit is given by $v_D = \sqrt{2\hbar\gamma/M}$ (full width). For our transition $v_D = 0.55$ m/s, and is well below the final distribution width attained with BF cooling. However, the Doppler molasses capture range is also restricted to $v_c = 2\gamma/k = 1.16$ m/s (full width), resulting in a maximum velocity space compression by a factor of about 2. By contrast, the BF cooling has a velocity capture range determined by the experimental parameter δ (as opposed to the atomically determined γ) allowing a much greater velocity space compression. It is also important to note that the BF is able to accomplish this in a shorter time (Doppler cooling requires many spontaneous emissions).

We assert that these characteristics of Fig. 7 confirm our hypothesis that *laser cooling is indeed possible* on a time scale where *spontaneous emission cannot make a significant contribution* [4–6].

IV. SUMMARY AND CONCLUSIONS

We have presented the results of a series of numerical simulations of laser cooling by the BF for conditions that match the experimental conditions of Refs. [4,6]. The accuracy of the simulation was first tested with velocity-space trajectories for the more commonly used single-frequency optical fields. Next, similar trajectories for the BF were calculated with an interaction time of 300 ns, and these showed sensitivity to the initial conditions (z_0 and t_0) of atoms in the light field. For meaningful comparison with our experiments, this required

calculating many trajectories over a span of initial conditions to match the uncontrolled experimental conditions.

The simulations also included the severe effects of the atomic longitudinal velocity distribution on the time-of-flight detection technique, as well as those of the different transition strengths arising from the multiple magnetic sublevels of the involved states. The experiment cannot be simultaneously optimized for these different strengths.

The simulation has reproduced the main features of the measurements of Ref. [4], and provides additional support for the idea of laser cooling without spontaneous emission using the BF. Additionally it shows cooling even when spontaneous emission does occur as shown in Fig. 3. Thus for systems that wish to reduce the effects of spontaneous emission, the BF is a good candidate. Radiative laser cooling typically requires multiple absorption-spontaneous emission cycles. However, the BF can produce cooling without spontaneous emission, and occasional spontaneous emission events do not hinder the cooling process. This could be particularly helpful for the direct laser cooling of molecules without closed cycling transitions. While spontaneous emission to additional states requiring repumping may sometimes be necessary, the BF would reduce the level of repumping required. Moreover, the huge strength of the BF enables cooling in tightly confined spaces and/or very short times [1].

We assert here that these results should further remove the widespread controversy about laser cooling without spontaneous emission [4–6].

ACKNOWLEDGMENTS

We thank Martin G. Cohen for careful reading of the manuscript and multiple suggestions. This work was supported by the ONR.

-
- [1] J. Söding, R. Grimm, Y. B. Ovchinnikov, P. Bouyer, and Ch. Salomon, *Phys. Rev. Lett.* **78**, 1420 (1997).
 - [2] M. R. Williams, F. Chi, M. T. Cashen, and H. Metcalf, *Phys. Rev. A* **61**, 023408 (2000).
 - [3] L. Yatsenko and H. Metcalf, *Phys. Rev. A* **70**, 063402 (2004).
 - [4] C. Corder, B. Arnold, and H. Metcalf, *Phys. Rev. Lett.* **114**, 043002 (2015).
 - [5] H. Metcalf, *Phys. Rev. A* **77**, 061401(R) (2008).
 - [6] C. Corder, B. Arnold, X. Hua, and H. Metcalf, *J. Opt. Soc. Am. B* **32**, B75 (2015).
 - [7] M. Partlow, X. Miao, J. Bochmann, M. Cashen, and H. Metcalf, *Phys. Rev. Lett.* **93**, 213004 (2004).
 - [8] C. S. Allred, J. Reeves, C. Corder, and H. Metcalf, *J. Appl. Phys.* **107**, 033116 (2010).
 - [9] H. Metcalf and P. van der Straten, *Laser Cooling and Trapping* (Springer, New York, 1999).
 - [10] J. Söding, Ph.D. thesis, MPI–Kernphysik, University of Heidelberg, 1996.
 - [11] M. A. Chieda and E. E. Eyler, *Phys. Rev. A* **84**, 063401 (2011).
 - [12] S. E. Galica, L. Aldridge, and E. E. Eyler, *Phys. Rev. A* **88**, 043418 (2013).
 - [13] L. Aldridge, S. E. Galica, and E. E. Eyler, *Phys. Rev. A* **93**, 013419 (2016).
 - [14] C. Salomon, J. Dalibard, A. Aspect, H. Metcalf, and C. Cohen-Tannoudji, *Phys. Rev. Lett.* **59**, 1659 (1987).
 - [15] J. Dalibard and C. Cohen-Tannoudji, *J. Opt. Soc. Am. B* **2**, 1707 (1985).
 - [16] E. Kyrola and S. Stenholm, *Opt. Commun.* **22**, 123 (1977).
 - [17] V. Minogin and O. Serimaa, *Opt. Commun.* **30**, 373 (1979).